Coseismic slip model of the 2008 Wenchuan earthquake derived from joint inversion of interferometric synthetic aperture radar, GPS, and field data

Xiaopeng Tong,[1] David T. Sandwell,[1] and Yuri Fialko[1]

[1]   We derived a coseismic slip model for the M_w 7.9 2008 Wenchuan earthquake on the basis of radar line-of-sight displacements from ALOS interferograms, GPS vectors, and geological field data. Available interferometric synthetic aperture radar (InSAR) data provided a nearly complete coverage of the surface deformation along both ascending (fine beam mode) and descending orbits (ScanSAR to ScanSAR mode). The earthquake was modeled using four subfaults with variable geometry and dip to capture the simultaneous rupture of both the Beichuan fault and the Pengguan fault. Our model misfits show that the InSAR and GPS data are highly compatible; the combined inversion yields a 93% variance reduction. The best fit model has fault planes that rotate from shallow dip in the south (35°) to nearly vertical dip toward the north (70°). Our rupture model is complex with variations in both depth and rake along two major fault strands. In the southern segment of the Beichuan fault, the slip is mostly thrust (<13 m) and occurred principally in the upper 10 km of the crust; the rupture progressively transformed to right-lateral strike slip as it propagated northeast (with maximum offsets of 7 m). Our model suggests that most of the moment release was limited to the shallow part of the crust (depth less than 10 km). We did not find any "shallow slip deficit" in the slip depth distribution of this mixed mechanism earthquake. Aftershocks were primarily distributed below the section of the fault that ruptured coseismically.

1.   Introduction

[2]   On 12 May 2008, a major (M_w 7.9) earthquake struck Wenchuan County, Sichuan Province, China. The casualties include approximately 70,000 dead and 374,000 injured. The rupture accompanying the event extended over 270 km toward the northeast along Longmen Shan thrust belt and was a result of the convergent tectonic movement between Tibetan Plateau and Sichuan Basin (Figure 1). The region of the earthquake is characterized by a 3 km topographic step across the rupture zone from the relatively flat lowlands of the Sichuan basin to the east to the rugged highlands of the Longmen Shan to the west [*Burchfiel et al.*, 2008].

[3]   The interseismic Global Positioning System (GPS) data collected between 1991 and 1998 reveal low shortening rate (<3 mm/yr) across Longmen Shan fault zone [*Chen et al.*, 2000]. Geologic and geomorphologic observations suggest that the parallel Beichuan (also referred to as Yingxiu-Beichuan fault) and Pengguan faults are active and dominated by dextral-slip structures [*Kirby et al.*, 2003; *Densmore et al.*, 2007]. The 2008 event started at the southern end of Beichuan fault at depth around 16 km [*Huang et al.*, 2008] and propagated toward northeast. Geological survey found that surface rupture occurred on two parallel fault strands: Beichuan fault (240–270 km) and Pengguan fault (70 km) (Figure 1). The survey established that the surface rupture is extensive with an average offset of 2 m. The maximum reported vertical throw is 6 m, and the maximum horizontal offset is 4.9 m [*Liu-Zeng et al.*, 2009]. There were 2706 events with a magnitude above 2.0 following the main shock by the end of 8 July 2008. Double difference relocation reveals that 95% of aftershocks were distributed over a depth interval of 10 to 20 km below the Earth's surface [*Huang et al.*, 2008]. The coseismic displacements due to the 2008 event were studied using synthetic aperture radar (SAR) pixel-tracking method [*Kobayashi et al.*, 2009] as well as interferometric synthetic aperture radar (InSAR) [*Hao et al.*, 2009]. Although the measurement accuracy is limited, *Kobayashi et al.* [2009] demonstrated that the rupture involved both the Beichuan fault and the Pengguan fault, consistent with the decorrelation zone in radar interferograms (as discussed below) and the geological survey

---

[1]Institute of Geophysics and Planetary Physics, Scripps Institution of Oceanography, La Jolla, California, USA.
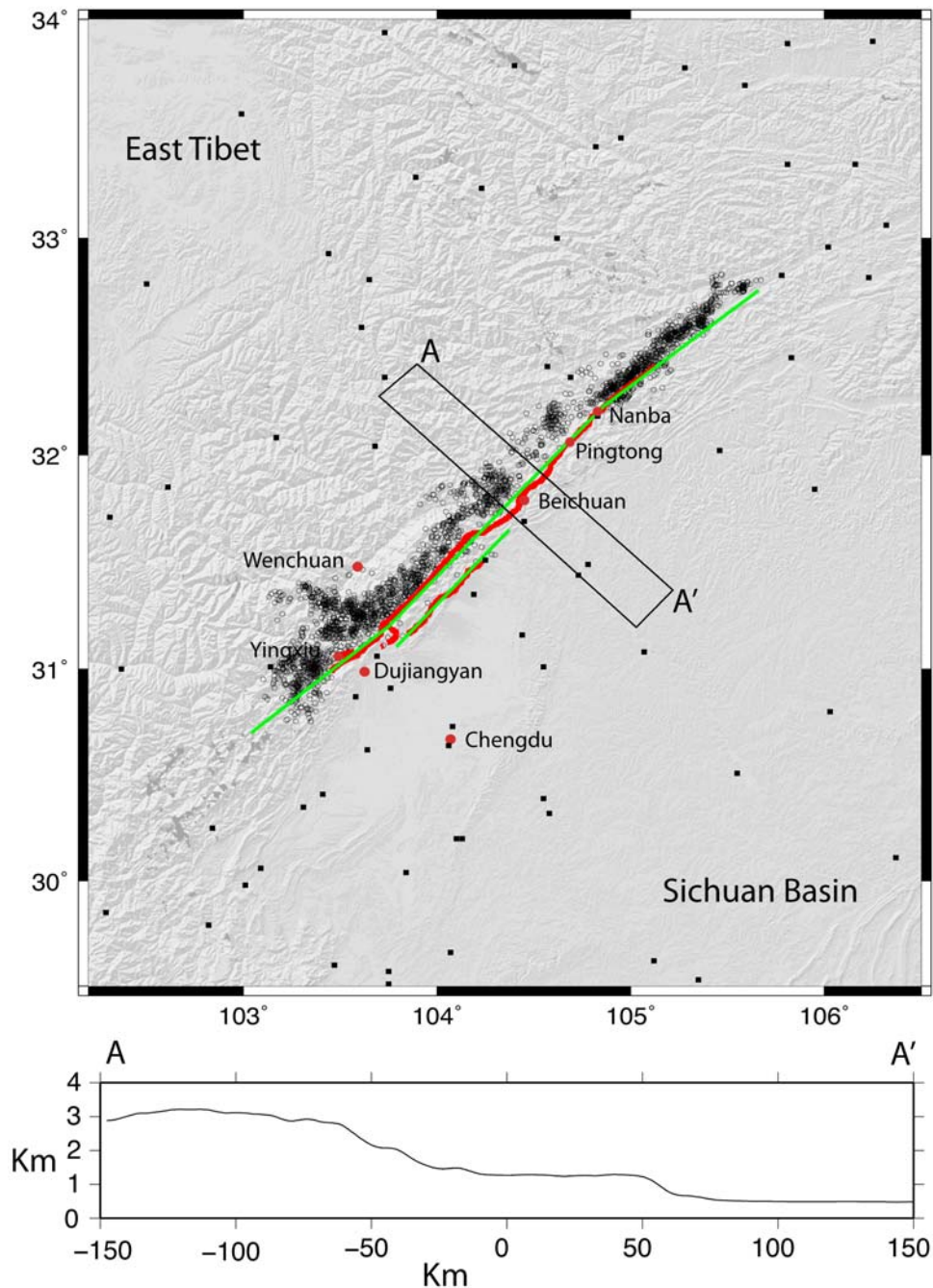
Figure 1. (top) Shaded topography in the Longmen Shan area. The black circles are 2706 relocated aftershocks ($M > 2.0$) that followed the main shock by the end of 8 July 2008 [*Huang et al.*, 2008]. The red line is the surface rupture from a geological survey [*Liu-Zeng et al.*, 2009]. The green lines indicate four segments of simplified faults used in the inversion. The black squares show the deployed GPS receivers [*Working Group of the Crustal Motion Observation Network of China Project*, 2008]. (bottom) The filtered topographic step across Longmen Shan fault zone.

[*Liu-Zeng et al.*, 2009]. Studies based on teleseismic and GPS observations indicate that the coseismic motion involved both thrust and dextral slip components [*Ji and Hayes*, 2008; *Working Group of the Crustal Motion Observation Network of China Project*, 2008] but the spatial variations of the right-lateral strike slip and dip slip, along with the depth distribution of fault slip, are not well constrained. The more recent InSAR analysis [*Hao et al.*, 2009] using seven ascending tracks of Advanced Land Observation Satellite (ALOS) Phase Array L-band Synthetic Aperture Radar (PALSAR) data revealed significant change in slip magnitude and direction along the rupture surface.

[4] In this study, we integrate InSAR data collected by the ALOS satellite (both ascending and descending), Global Positioning System (GPS) data, and geological field observations, along with Green's functions for an elastic

Table 1. Acquisition Dates, Perpendicular Baselines, and Planar Phase for Each Interferometry Track

	Track						
	471	472	473	474	475	476	124 (ScanSAR)
Acquisition dates	29 Feb 2008 to 31 May 2008	28 Jan 2008 to 17 Jun 2008	17 Feb 2008 to 19 May 2008	5 Mar 2008 to 5 Jun 2008	20 Jun 2007 to 22 Jun 2008	8 Apr 2008 to 24 May 2008	3 Jan 2008 to 20 May 2008
Maximum perpendicular baseline[a] (m)	93.2	211.6	229.5	290.7	68.4	207.0	920.6
Planar phase removed[b]							
Sx (rad/deg)	−15	6	−6	0	−3	−3	0
Sy (rad/deg)	−15	12	0	0	−6	−4	5
DC value (rad)	4.79	−2.66	2.13	1.06	−1.06	−6.39	3.19

[a]The baseline for each scene along every track varies slightly due to the long range of the curved satellite orbit.
[b]The details about the planar phase are discussed in the text.

half-space [*Okada*, 1985], to derive a coseismic slip model for the Wenchuan earthquake. The model allows for spatially variable rake angles and illustrates relative contributions of the thrust and strike-slip motion in the deeper part of the fault, as well as the along-strike variability. The inferred slip distribution can be used as a constraint in time-dependent inversions using seismic data [*Hernandez et al.*, 1999; *Delouis et al.*, 2002] and in studies of the coseismic stress changes [*King et al.*, 1994] and as an initial condition to drive models of postseismic relaxation [*Pollitz et al.*, 2000; *Hearn et al.*, 2002; *Fialko*, 2004b; *Perfettini and Avouac*, 2007; *Barbot et al.*, 2009]. The latter can be compared to the geodetic data collected after the earthquake to constrain the relaxation mechanisms and effective rheology and to provide insights into time-dependent stress transfer and future seismic hazard.

2. Data Analysis

[5] Rugged topography of the region combined with high rainfall and dense vegetation severely limits the correlation of C band interferograms to only the flat lowland areas. In contrast, adequate interferometric correlation is maintained in the longer wavelength L band SAR imagery provided by the PALSAR aboard the ALOS satellite [*Rosenqvist et al.*, 2007]. After the launch of ALOS by Japanese Aerospace Exploration Agency (JAXA) in January 2006, a global background mission collected strip-mode SAR imagery approximately four times per year on ascending tracks and scanning synthetic aperture radar (ScanSAR) imagery four times per year on descending tracks. The improved correlation at L band along with systematic preearthquake coverage enabled excellent coseismic InSAR coverage of the entire rupture zone. With the help of the Alaska Satellite Facility and JAXA, we assembled 78 scenes in fine beam single polarization (FBS) and fine beam dual polarization (FBD) mode from ascending orbit as well as four

scenes in ScanSAR mode from descending orbit [*Tong et al.*, 2008]. Topographic data, needed to perform the phase correction to the interferometry, were provided by the SRTM-3 data [*Farr et al.*, 2007]. The majority of void areas in the mountains have been filled from the best available alternative sources, including topographic maps, spot elevations on sketch maps and Landsat images [www.viewfinderpanoramas.org/dem3.html]. In addition to the InSAR data, we incorporated 109 GPS vectors (82 horizontal and 27 vertical) [*Working Group of the Crustal Motion Observation Network of China Project*, 2008] and geological field observations [*Liu-Zeng et al.*, 2009] as ground truth constraints.

2.1. InSAR Data Processing

[6] We used SIOSAR software to process ALOS PAL-SAR data [*Sandwell et al.*, 2008]. We chose the SAR images from the available archive immediately following the earthquake as the repeat scenes, then search back in time to get the reference scenes with optimal baselines. The time span of the interferograms ranges from 46 days to 1.5 years; the latest one after the earthquake is on 22 June 2008, about 40 days after the main shock (Table 1). We assume coseismic signal dominates any postseismic response that may have occurred during interval between the main shock and the first repeat acquisition on each track. The perpendicular baselines vary between 70 and 844 m and the longer perpendicular baseline are more sensitive to topography. The short baselines along the ascending tracks help to reduce the topographic effect, which may obscure the surface deformation. The interferograms are processed frame by frame (six to eight frames per track) to improve image matching and keep file sizes manageable. Individually processed interferograms mosaic seamlessly along the same track in either radar or geographic coordinates (Figure 2). A spatial Gaussian filter

Figure 2. (a) Ascending swath mode interferograms after trend removal (six tracks). The color scale shows the wrapped phase that corresponds to the range change (11.8 cm per fringe) between the ground points to the radar antenna. Phase increase corresponds to range increase, and vice versa. The red star is the main shock, and the two red dots are two M6.0 aftershocks. The red line is the surface rupture from geological survey. The zoom view demonstrates the fine phase fringes on the hanging wall that are manually digitized. (b) Descending ScanSAR mode interferograms after trend removal (11.8 cm per fringe). Each scene of the interferogram consists of five subswaths across look direction. The decorrelation in the mountainous area is probably due to the long perpendicular baseline (657–844 m). The phase change has the same sign as the range change, in the same convention as in Figure 2a. The zoom view emphasizes the fine phase fringes on the footwall.
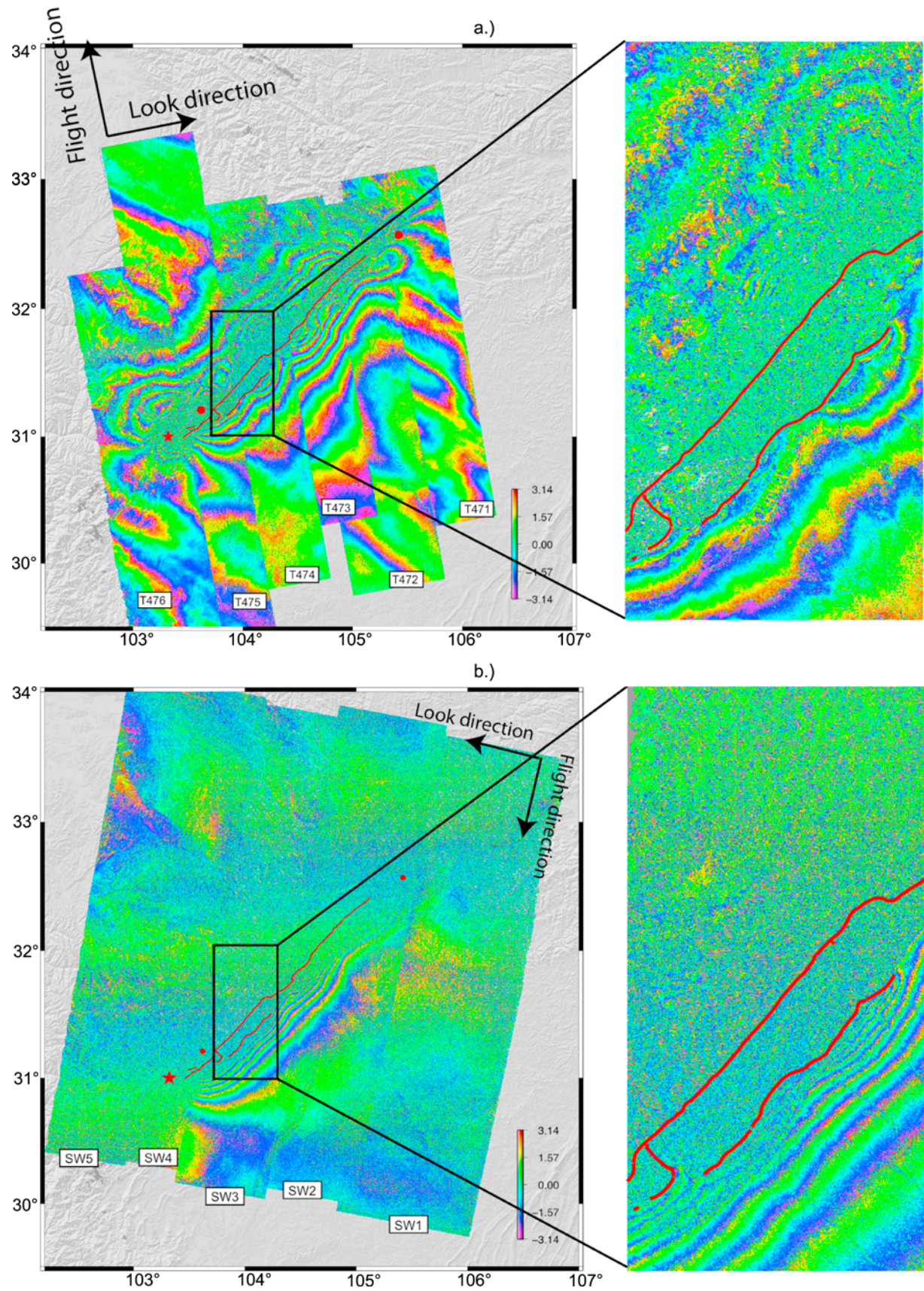
Figure 2

having a 0.5 gain at 300 m wavelength was applied to all the interferograms [*Sandwell et al.*, 2008]. This cutoff wavelength is a compromise between greater smoothing for improved correlation in areas of extreme ground shaking and less smoothing to recover the high fringe rate caused by deformation near the rupture.

[7] As well demonstrated by previous studies, more than one radar look direction is needed to provide reliable estimates of slip along a rupture [*Fialko et al.*, 2001; *Sandwell et al.*, 2002; *Simons et al.*, 2002; *Fialko*, 2004a]. In the case of ALOS, normal strip-mode interferometry is available on ascending orbits but along the descending orbits the only acquisitions are in the ScanSAR mode. We processed four ScanSAR scenes (track 124, frame 2950 and 3000) to provide additional line-of-sight (LOS) displacement measurements, though the long perpendicular baselines (657–844 m) along descending track led to complete decorrelation in the mountainous area (Figure 2b). This is the first PALSAR ScanSAR to ScanSAR interferogram constructed by our group so we discuss the technical details of this development in Appendix A.

2.2. Interpretation of Interferograms

[8] Figure 2 shows the mosaics of 39 ascending and 2 descending radar interferograms in wrapped phase with a full coverage of 400 km by 400 km along the Longmen Shan fault zone. A zoom view of the interferogram illustrates dense phase fringes close to the rupture zone that document a complicated pattern of surface deformation. The speckled area in the interferograms denotes regions of decorrelation. The red line is the surface rupture mapped by Jing Liu from the Chinese Academy of Sciences [*Liu-Zeng et al.*, 2009]. The mapped faults align very well with the edge of the decorrelation near the fault zone: on east side of the faults, corresponding to the footwall, phase is recoverable all the way to the fault trace; on the west side, corresponding to the hanging wall, the signal is completely decorrelated. This is consistent with geologic and seismic observations showing that most of the ground shaking was concentrated on the hanging wall. While the lowland areas have good phase coherence, the phase recovery is less robust in the mountainous areas. Lower coherence on the hanging wall within 30 km of the fault zone is due to a combination of landsides, temporal decorrelation from vegetation, and inadequate topographic phase correction in the area of extreme relief. By directly counting the interferometric fringes and assuming zero displacement in the far field, we found that the peak LOS displacement in the ascending orbits is 99.4 cm on the hanging wall, −108.2 cm on the footwall; the peak LOS displacement in the descending orbits is −118.1 cm on the footwall.

2.3. Errors and Trends in Interferograms

[9] We need to consider and mitigate the potential spurious contributions to the radar phase before interpreting it as coseismic surface displacements. There are several factors that prevent us from directly relating the interferogram to surface deformation signal [e.g., *Massonnet and Feigl*, 1998]. The error sources come from the topographic phase correction, propagation effects due to the ionosphere and atmosphere, as well as orbital errors. The atmospheric propagation errors, mostly attributed to the tropospheric water

vapor content, are small (<5 cm) compared to the deformation due to the earthquake. No good atmospheric model is available to correct for the propagation delays, and they are not considered further.

[10] The topographic error is potentially important for this region because of the high elevation and rugged topography of the Longmen Shan (Figure 1) coupled with the relatively long perpendicular baseline of ALOS. Artifact fringes introduced by the topography are directly proportional to the error in the elevation model. SRTM-3 has a spatial resolution of 90 m outside North America and the vertical accuracy varies from 5 m in relatively flat areas to perhaps as much as 50 m in extreme terrain such as the Longmen Shan where there are gaps in SRTM coverage. This topography error h maps into a LOS displacement error l according to the following formula

$$\frac{\partial l}{\partial h} = \frac{R_e B_{perp}}{\rho b \sin \theta} \tag{1}$$

where R_e is the radius of the Earth, B_{perp} is the perpendicular baseline, ρ is the range from the satellite to the topography, b is the orbital radius of the spacecraft, and θ is the look angle. Note that this error is independent of radar wavelength. Using parameters appropriate for PALSAR with a 34.3° look angle and a 400 m perpendicular baseline, the ratio of range change rate to height is 7.6×10^{-4}. Therefore a 50 m topography error produces a LOS error of 3.8 cm (a fraction of a fringe), which can have an effect on the interpretation of the interferograms especially near the rupture zone, where there are significant changes in elevation. Moreover several interferograms have baselines that are larger still and the baseline of the ScanSAR interferogram is from 657 to 844 m. In this case, the LOS errors due to topography are large enough to cause complete decorrelation of the interferograms in the highland area.

[11] We suspect the clear stripe pattern in the northern part of the longer 475 track is associated with the ionospheric anomaly. Interestingly, this phase disturbances are more common on ascending orbits (2230 LT) than on descending orbits (1030 LT), which could be explained by the TEC decay in the nighttime. The plasma in the ionosphere can alter the refractive index and cause a frequency-dependent phase shift on microwave signals. The correspondent range shift is inversely proportional to the frequency; thus. it is 4 times larger at L band than at C band [*Meyer et al.*, 2006]. We attempted, without much success, to account for the large-scale ionosphere effect using the TEC from Global Ionosphere Maps (http://iono.jpl.nasa.gov/gim.html) by removing a phase ramp from our interferograms with a single-layer model.

2.4. Extracting Deformation From the Phase Data

[12] As discussed above the large-scale ionospheric and orbital errors produce phase ramps across the image that need to be removed before interpreting interferograms in terms of ground deformation. This trend estimation usually is performed after unwrapping the phase and simultaneously with model inversion. However, the decorrelation of the interferograms in mountains combined with shadowing and layover effect prevents a robust automatic phase unwrapping, especially in the areas of high phase

gradient near the rupture [*Goldstein et al.*, 1988; *Zebker et al.*, 1994; *Goldstein and Werner*, 1998]. In addition, much of the rupture zone is decorrelated so it is difficult to resolve the phase cycle ambiguity across the fault without counting fringes on adjacent swaths (Figure 2a). The problem is complicated by the fact that different swaths have phase ramps that need to be estimated concurrently. To mitigate the unwrapping problems we digitize the fringes manually and converted them to displacement in the LOS direction. Each fringe represents 11.8 cm of LOS motion. Note that the spacing between fringes is inversely proportional to the local phase gradient so the digitized data will be naturally focused in areas of high displacement gradient [*Simons et al.*, 2002]. Moreover, based on the a posteriori misfit of the model to the data, we find that the RMS error is typically one fringe (11 cm) so digitizing at one fringe interval appears to be adequate.

[13] We performed a two-stage digitization procedure to account for the ambiguity of phase steps across the fault and between neighboring swaths. Fringes furthest from the fault zone, representing the smallest LOS displacement were digitized first and we tracked toward the near-fault regions of very high phase gradient (Figure 2). We were able to count fringes in the partially decorrelated mountain region where automatic unwrapping scheme such as the Goldstein method does not work [*Goldstein et al.*, 1988; *Zebker et al.*, 1994; *Goldstein and Werner*, 1998]. After generating a preliminary slip model with this digitized data set, we removed the model interferogram (projected into the range-dependent LOS) from each track and then flattened the residual phase by fitting a planar trend to the far-field signal (Table 1). This planar phase correction (utilizing three model parameters) applied to each track dramatically improves the track-to-track continuity of fringes. These detrended interferograms were redigitized and converted to the LOS displacement to form our final InSAR data set. It consists of 5738 digitized LOS displacements from two different look directions, 729 points from the descending track and 5009 points from the ascending tracks. Note that the spatial sampling of the digitizing along each fringe is finer than the fringe spacing so the data are not linearly independent. Figure 3a and 3b show significant and complex deformation along the strike of Longmen Shan fault zone. The spatial gradients of the LOS displacements in cross-fault direction reach at least 2×10^{-5} in interferograms from both the ascending and descending orbits. We complement the InSAR measurements with 109 GPS observations and geological scarp height measurements from filed studies to constrain the coseismic slip model over a wide range of length scales.

3. Inversion for the Coseismic Slip Model

[14] We used the geologically mapped surface rupture and aftershock distribution to approximate the earthquake fault with four planar subfaults with different strike and dip angles. We used a relationship between slip on a fault patch and surface displacement assuming a homogeneous elastic half-space approximation [*Okada*, 1985; *Fialko*, 2004a]. The fault was parameterized using 280 patches (560 strike- and dip-slip components). The forward matrix relating slip on each patch to the observations consists of both the

Green's functions and smoothing matrix. The observation vectors d_{LOS} and d_{GPS} consist of the InSAR data, which are the LOS displacement from the ascending and descending tracks, and the GPS data with east-north-up displacement components. The model vectors m_{dip} and m_{strike} represent dip-slip and strike-slip components on discrete fault patches. The Green's functions for the full vector field are calculated given a prior fault parameterization, and are subsequently projected into LOS direction,

$$\begin{bmatrix} G_{LOS} \\ G_{GPS} \\ \lambda S \end{bmatrix} \begin{bmatrix} m_{dip} \\ m_{strike} \end{bmatrix} = \begin{bmatrix} d_{LOS} \\ d_{GPS} \\ 0 \end{bmatrix} \quad (2)$$

The regularization (smoothness) constraint minimizes the first derivative of slip (as approximated by a finite difference quadrature, see equation (3)) (for details, see *Fialko* [2004a]). Parameter λ in equation (2) is the weight of smoothing chosen based on a number of simulations to obtain the smoothest model that does not degrade the fit to the data.

$$S = \begin{pmatrix} 1 & -1 & 0 & 0 & \dots \\ 0 & 1 & -1 & 0 & \dots \\ 0 & 0 & 1 & -1 & 0 \\ \hdots \end{pmatrix} \quad (3)$$

3.1. Model Settings: Fault Geometry and Parameters

[15] The fault geometry is based on geological mapping of the surface rupture [*Liu-Zeng et al.*, 2009] and the relocation of aftershocks [*Huang et al.*, 2008]. We use three rectangular fault segments to approximate the Beichuan fault and one segment to approximate the southern part of the Pengguan fault (also referred to as the Guan Xian-An Xian fault). Each segment is further discretized into slip patches; see *Fialko* [2004a] for details. In the top row, slip patches are 4 km long and 2 km wide. The width of the patches increases progressively with depth by a factor of 1.5 (Figure 4) to maintain a uniform model resolution. While the surface trace of the fault is straightforward to define based on field mapping and SAR data, the dip angles of the fault segments are more difficult to determine. After testing the sensitivity of the RMS of the model residuals to the overall fault dip with help of a grid search method (Figure 5), we found that the available data are consistent with the fault dip within a wide range of 40°–60°. We note that the seismicity is not localized on a narrow fault plane, which may reflect the complex fault geometry at depth in this region. To account for a possibility of a spatially variable dip angle, we solve for the dip angles of each segment separately using the grid search method (see Figure 5 for details). The best fit model has fault planes that rotate from shallow dip in the south (35°) to nearly vertical dip toward the north (70°). This result is in a general agreement with the relocated aftershocks [*Huang et al.*, 2008]. After several iterations, we fix the fault geometry before final inversion for slip on each patch (Table 2). The inversion requires subsurface slip well beyond the ends of the surface rupture on the Beichuan Fault and Pengguan Fault segments. The maximum depth
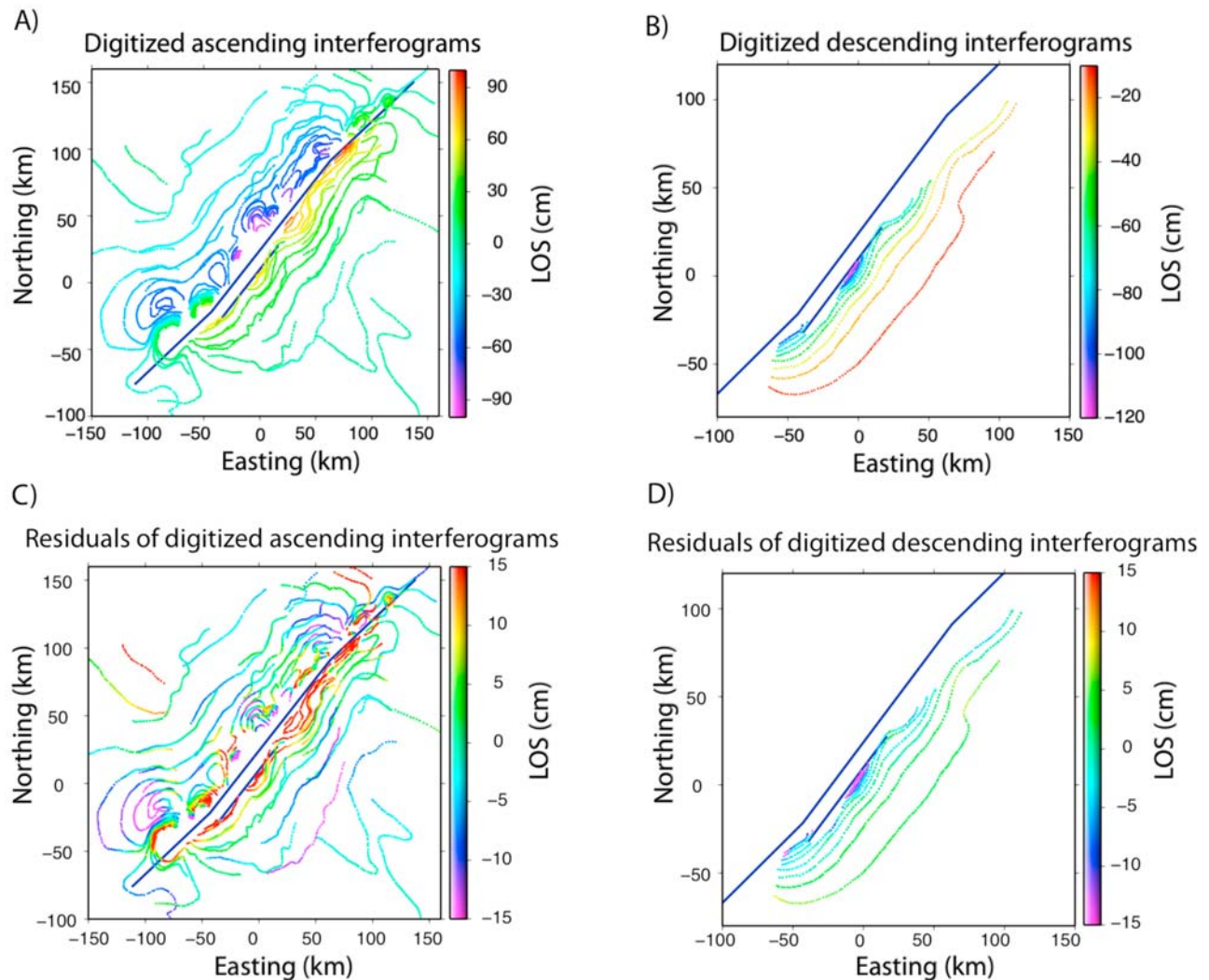
Figure 3. (a and b) Digitized InSAR data in map view. Each line of dots represents the digitized fringes with an integer phase value in the interferograms. The color represents the line-of-sight (LOS) displacement. (c and d) The model residuals. Positive LOS displacement represents decrease in the distance from ground scatters to the radar; negative LOS displacement represents increase in the distance from ground scatters to the radar. Note the LOS displacement is a combination of the horizontal and vertical components.

of each fault plane was limited to 25 km, which corresponds to the depth extent of aftershocks (see Figure 10); deeper slip is not required by the InSAR and GPS data.

3.2. Topographic Effect

[16] The Wenchuan earthquake occurred along the steepest topographic gradient of the Longmen Shan thrust belt (Figure 1) [*Densmore et al.*, 2007]. The mountains to the northwest are on average 3 km higher than the Sichuan Basin to the southeast at 500 m elevation. This elevation contrast is sufficiently large that we need to take it into account in our inversion. In modeling the topographic effects, we set 500 m above from sea level as the reference (free surface of the half-space) and modify the Green's functions according to the elevation of each data point. For points above this level the effective depth of slip

Figure 4. Coseismic slip model. (a) The total slip magnitude on fault patches (represented by the color). The faults are located as shown in the inset map. The white lines, which originate from center of the rectangular patches and point outward, illustrate the relative motion of the hanging wall with respect to the footwall (thrust slip and right-lateral strike slip in this case.) One can imagine standing on the northwest side of the fault and looking southeastward. The yellow star is the main shock. Note that the dip angles of the fault planes are different (Table 2). (b) The dip-slip magnitude on fault patches (represented by the color). Note that the diminished dip slip on the southern end of middle Beichuan fault is less robust due to ambiguity in the slip partitioning. (c) The strike-slip magnitude on fault patches (represented by the color).
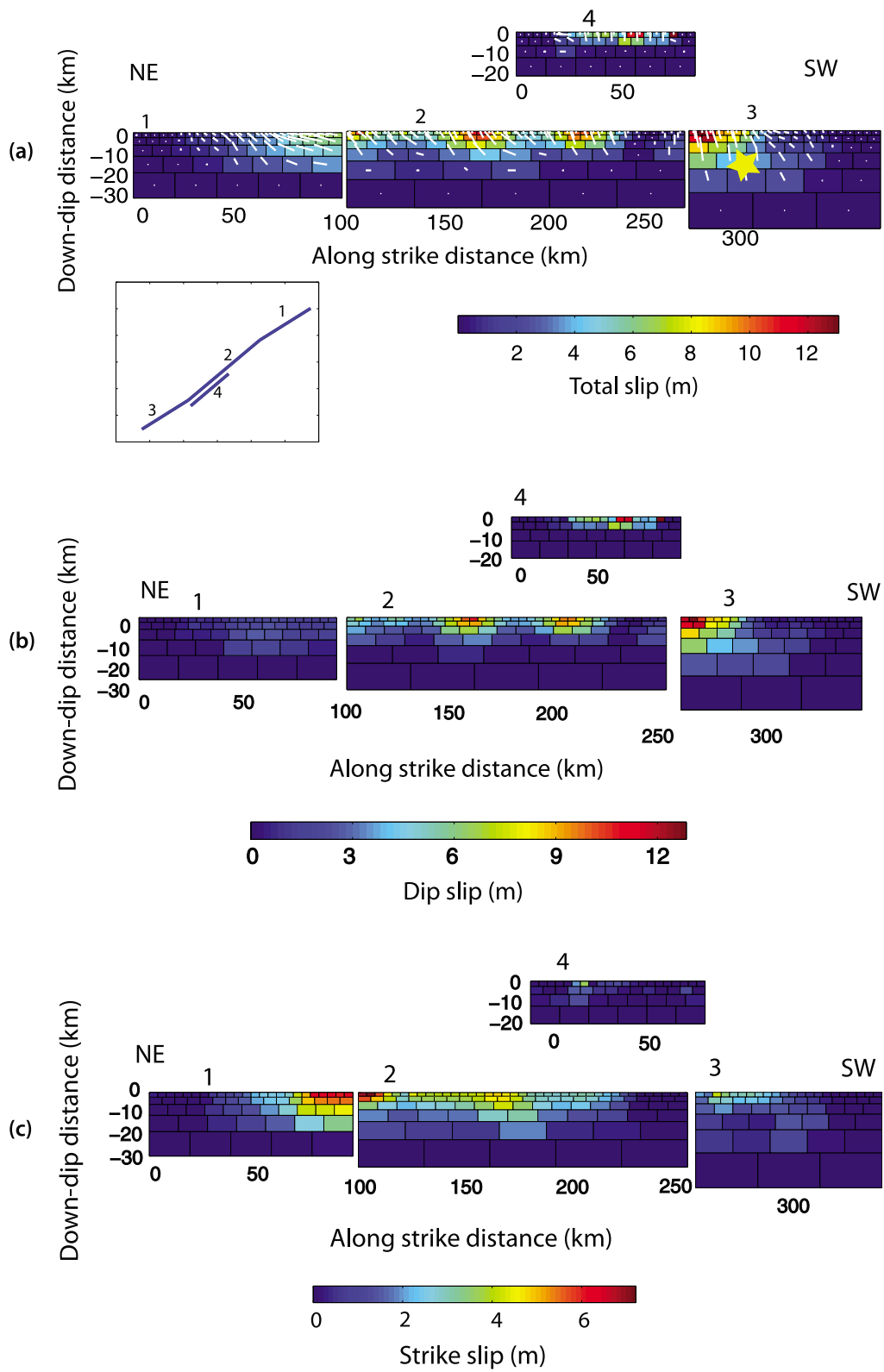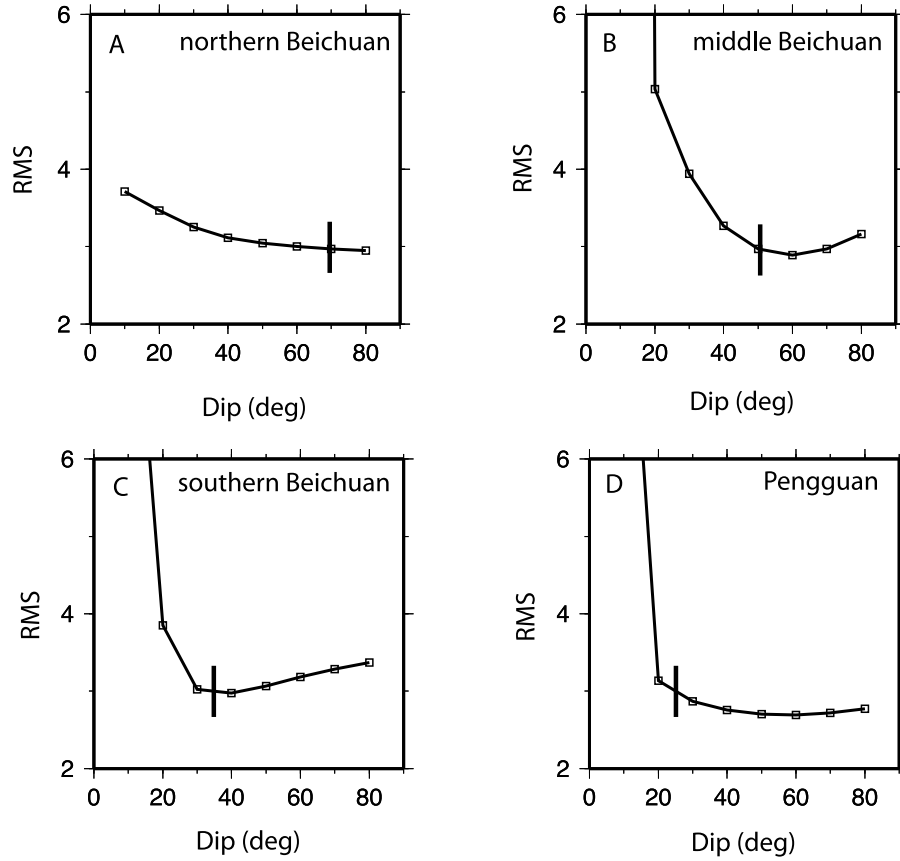
Figure 4

Figure 5. Plots of the normalized RMS misfit with various fault dip angles. We altered the dip angle of each fault segment at 10° intervals while keeping other parameters fixed in searching for optimal fault dips. The stick indicates the dip angles we used in our best fitting model. (a) The northern Beichuan fault, which is a nearly vertical fault. (b and c) The middle and southern Beichuan faults, which are fairly well constrained. (d) The Pengguan fault, which is the worse constrained: the dip angle can vary from 20° to 80°.

patches was increased when calculating the surface displacement. This first-order correction improved fit to the InSAR data on the hanging wall side of the fault.

3.3. Incidence Angle

[17] The incidence angle in radar interferograms varies smoothly from 16.8° to 44.1° along descending tracks and from 36.8° to 41.4° along ascending tracks. We utilize precise orbit data to calculate the unit look vectors in a global Cartesian coordinate system for each InSAR ground point measurement and then convert them into local east-north-up coordinates using rotation matrix [*Price and Sandwell*, 1998]. This information is needed for the inversion matrix. The observation vectors are given by

$$d_{los} = [d_E \quad d_N \quad d_V] \begin{bmatrix} n_E \\ n_N \\ n_V \end{bmatrix} \quad (4)$$

where d_{los} is the displacement in LOS direction; d_E, d_N, d_V are displacements in east, north, and up, respectively; n_E, n_N, n_V are three component of the unit look vectors.

3.4. Joint Inversion

[18] After applying weights on different data types according to the measurement errors in equation (2), terms in the combined linear system of equations to be solved are

$$A = \begin{bmatrix} \sigma_{LOS}^{-1} G_{LOS} \\ \beta \sigma_{GPS}^{-1} G_{GPS} \\ \lambda S \end{bmatrix}, \quad b = \begin{bmatrix} \sigma_{LOS}^{-1} d_{LOS} \\ \beta \sigma_{GPS}^{-1} d_{GPS} \\ 0 \end{bmatrix}, \quad m = \begin{bmatrix} m_{dip} \\ m_{strike} \end{bmatrix} \quad (5)$$

where σ_{LOS} and σ_{GPS} are two diagonal matrices derived from measurement uncertainties and β represents the relative weight of InSAR and GPS data sets. We minimize the

Table 2. Modeled Fault Geometry and Their Geographic Locations

	Fault Model Index			
	1	2	3	4
lon0[a]	105.26	104.31	103.40	104.08
lat0[a]	32.49	31.71	30.95	31.38
Strike (deg)	−128.41	−136.84	−128.43	−137.03
Dip (deg)	70	50	35	25
Length (km)	95.74	154.82	87.60	82.07

[a]The center of the top edge of each fault segment.
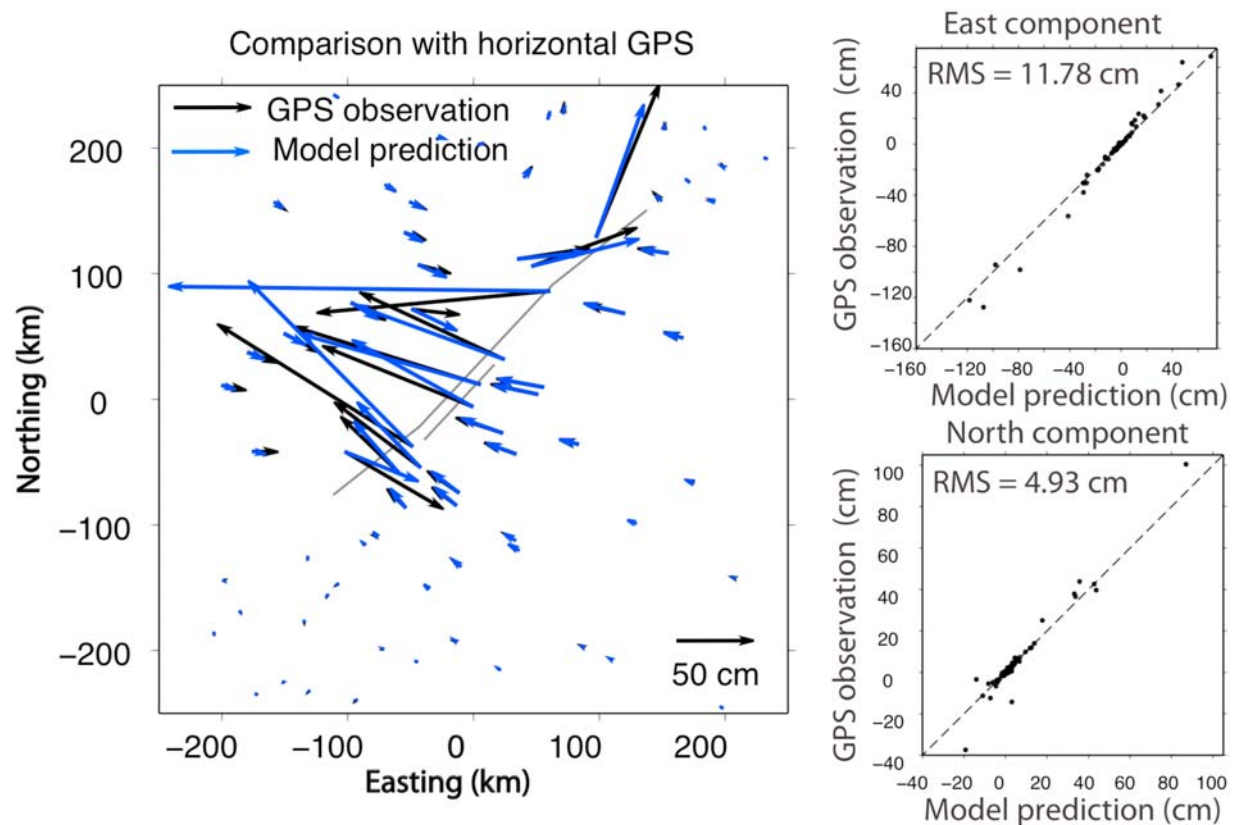
Figure 6. (left) The horizontal GPS measurements (black arrows) and our model prediction (blue arrows). (right) Model prediction versus GPS observation in (top) east and (bottom) north directions. The model residuals in the corner show the goodness of the fit. The larger RMS in east component could be due to larger magnitude of the east-westward movement. Gray lines are simplified fault models. The error ellipses on the GPS data are relatively too small to be seen [*Working Group of the Crustal Motion Observation Network of China Project*, 2008].

misfit between the data and the model prediction in a least squares sense subject to two types of constraints: the first one is the positivity constraint prohibiting normal and left-lateral slip on the fault. The positivity constraint prevents unphysical "Checker boarding" patterns. As shown in Figure 4c, the positivity constraint on strike slip is mostly redundant (see discussion below). The second constraint is invoked to satisfy the field data on scarp height along the fault,

$$\min \|Am - b\|$$
$$m_{dip} \geq 0, m_{strike} \leq 0, Cm \geq s \qquad (6)$$
$$C = G_{hanging} - G_{foot}$$

where s is the selected scarp height measurements on the surface rupture from geological survey [*Liu-Zeng et al.*, 2009] and C is the Green's function for the vertical component of the surface throw on the fault, which is the difference in vertical displacements between the hanging wall and the footwall. The scarp height might be underestimated due to the presence of secondary faulting; thus, we take the geologically measured scarp height as a lower bound. In other words, we added an inequality constraint that requires the model prediction of scarp height to be greater than the geologic observations. Equation (6) is a specific expression of the typical least squares problem with nonnegative constraint (NNLS) [*Lawson and Hanson*, 1974] that has numerically stable solutions [*Parker*, 1994].

[19] Calculated surface displacements are based on an elastic, isotropic and homogeneous half-space model. The Poisson ratio is taken to be 0.25. We used the trade-off curve between model smoothness and normalized RMS misfit to define optimal smoothness parameter. The relative weight between InSAR and GPS data sets is adjusted iteratively, and then fixed when the misfit reaches the minimum. Our best fitting model based on three independent data sets can explain both InSAR and GPS measurements reasonably well and results in a variance reduction of 93%.

[20] Figure 3 shows that the residuals between InSAR data and the model predictions (ascending interferograms with mean 2.30 cm, standard deviation 12.41 cm; descending interferograms with mean −1.52 cm, standard deviation 10.20 cm). The greater near-fault residuals might be due to a combination of complicated near-field deformation, early postseismic deformation, oversimplified fault geometry, and material heterogeneity. The same model also provides a good fit to the GPS observations (Figures 6 and 7). The RMS of the model residuals for GPS data is 4.93 cm for north component; 11.78 cm for east component; 6.75 cm for vertical component. Finally the model provides
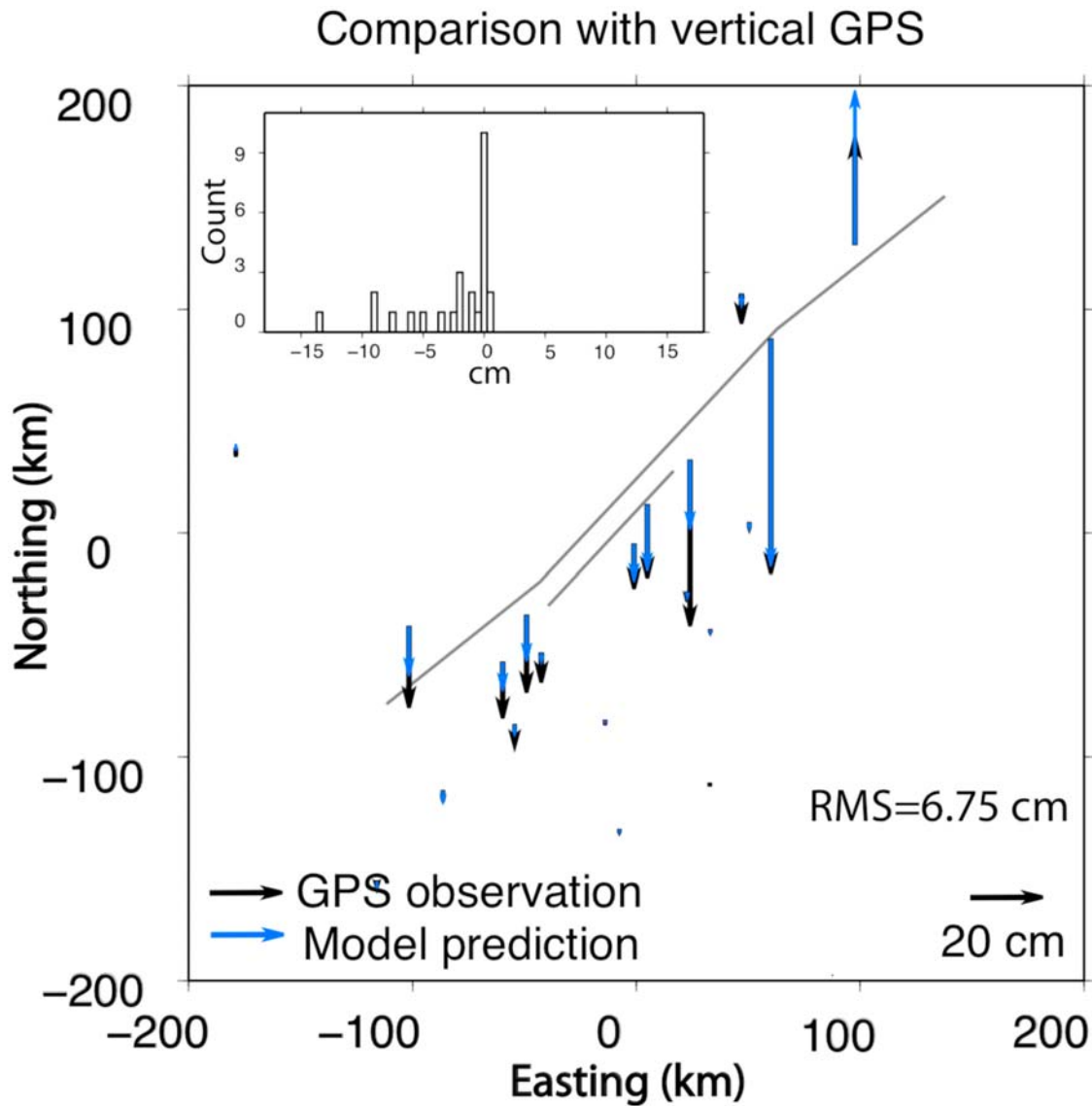
Figure 7. The vertical GPS measurements (black arrows) and the model predictions (blue arrows). The inset shows the distribution of the residuals.
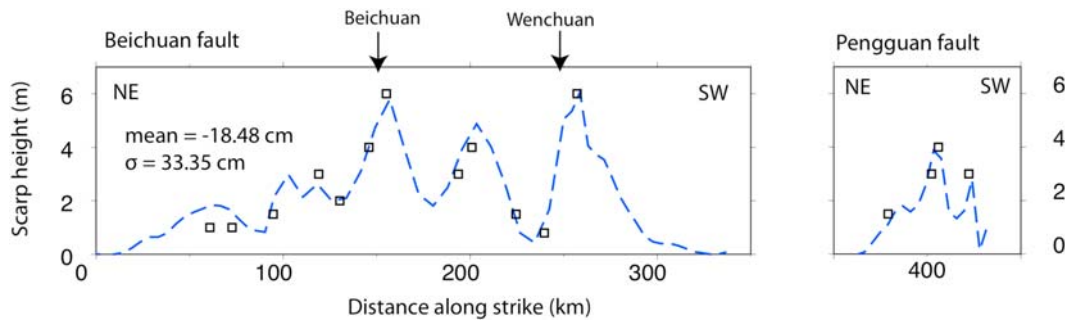
Figure 8. Selected scarp height measurements (black boxes) used in the inversion from the geological survey [*Liu-Zeng et al.*, 2009]. The blue dashed lines are the model predictions. The vertical offsets vary along the strike of the fault with peaks near Beichuan and Wenchuan areas. The model residuals have a mean value of −18.48 cm and a standard deviation of 33.35 cm.
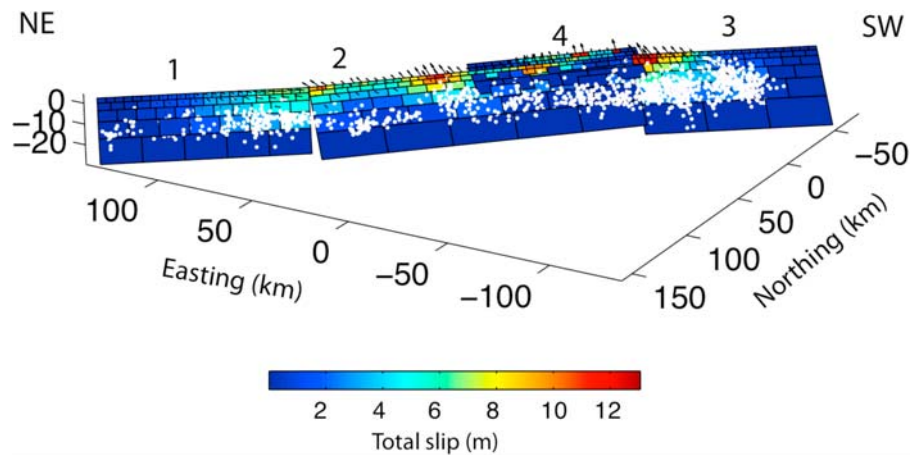
Figure 9. Coseismic slip model in 3-D view. The white dots are the aftershocks from double difference relocation result [*Huang et al.*, 2008].

a good match to the observed scarp height along the fault (see Figure 8) [*Liu-Zeng et al.*, 2009]. Figure 8 shows that the calculated vertical offsets along the Beichuan and Pengguan faults correlate well with the geologic measurements. The fault scarp height (i.e., vertical offset) varies along strike with peaks near Beichuan and Wenchuan areas, which suggests that the modeled coseismic slip in the shallow layers agrees with the geological observations. The magnitude of vertical displacement is also affected by fault dip angle at shallow depth, and the along-strike variation of vertical offsets could thus partially been due to change in fault dip along strike. We did not use the geologic lateral offset data in the inversions because they are subject to larger bias [*Liu-Zeng et al.*, 2009].

4. Results and Discussion

[21] The total geodetic moment inferred from our best fitting model is 6.79×10^{20} N m (equivalent to earthquake moment magnitude of 7.8), in general agreement with the 7.9 moment magnitude (seismic moment of 7.6×10^{20} N m) from U.S. Geological Survey. The geodetic moment is taken to be the vector sum of the strike-slip (3.61×10^{20} N m) and dip-slip (4.96×10^{20} N m) components, which are nearly equally partitioned. Caution should

be exercised when interpreting the estimated geodetic moment. First, to achieve a realistic geodetic moment, it involves estimating the area of rupture, the associated static slip and the shear modulus to a sufficient accuracy. Second, this geodetic moment should not be confused with the seismic moment because aseismic slip could take place after the dynamic rupture process and alter the final static deformation field.

[22] The coseismic slip model (Figures 4 and 9) based on a joint inversion of InSAR and GPS data shows the complex spatial variation in both depth and rake along the two major fault strands. The inferred subsurface rupture length is 304 km, which is consistent with the 316 km long distribution of aftershocks. On the Beichuan fault, the faulting in the epicentral area is dominated by a thrust component (5 to 13 m) and the major rupture extends down to depth of 10 km. The rupture progressively changed to strike slip as it propagated northeast. In its middle segment, the slip is shallower (8 km) and the amount of right-lateral strike slip and thrust are nearly equal (5 to 10 m for each component). On average, slip on the Beichuan fault extends to greater depth (12 km) toward the northern end and is mainly right-lateral strike slip (2–7 m). The Pengguan fault, which runs parallel to the Beichuan fault, is inferred to have dominantly thrust slip (<12 m) at very shallow

Table 3. Description of the Best Fitting Coseismic Slip Model

	Fault Plane Index			
	1	2	3	4
Fault segment	northern Beichuan	middle Beichuan	southern Beichuan	Pengguan
Maximum total slip amplitude (m)	7	12	13	12
Maximum slip depth (km)	23	22	21	7
Average slip depth (km)	12	8	10	3.5
Description of fault style	Rupture was mainly right-lateral strike slip, which peaked near surface, on the southern end of the fault.	Rupture was a combination of the right-lateral strike slip and thrust slip. The slip pattern was heterogeneous along strike and shallowly distributed.	Rupture was predominant thrust slip with intensive slip near surface on the northern end of the fault.	Rupture was predominant thrust slip near surface.
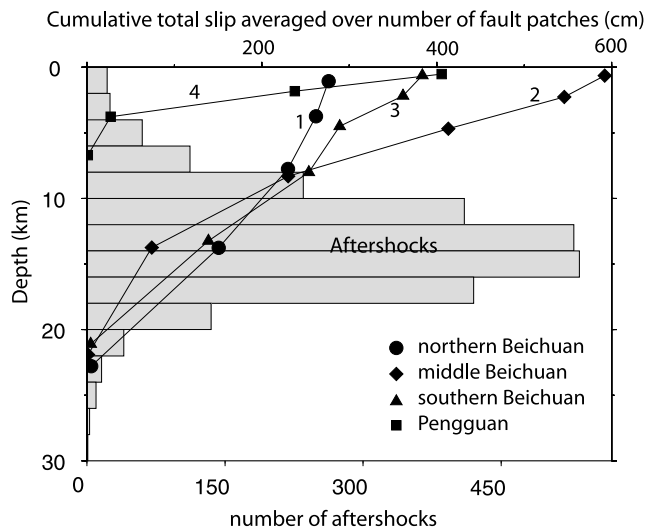
Figure 10. The amount of slip versus depth. The connected symbols indicate the normalized cumulative slip on the four fault segments (defined by $\Sigma_i\, S_i/L$, where S_i is the magnitude of total slip on each fault patch of one single layer and L is the correspondent number of the fault patches), whose scale is on the top horizontal axis. The index numbers (1 to 4) on each line correspond to different fault segments (Figure 4). The gray histogram shows the depth distribution of aftershocks [*Huang et al.*, 2008].

depth (see Table 3 for detailed summary). Figure 4 shows that the coseismic slip on the fault planes was heterogeneous along the strike: the thrust motion on the Beichuan fault concentrated near surface at a distance of 160, 210, and 260 km from the northeast end of the modeled fault plane. The dip slip reached more than 10 m in those high-slip areas (see Figure 4b). The right-lateral strike slip was mainly distributed in the northern part of the Beichuan fault near surface, at a distance of 50–100 km from the northeastern tip, with a magnitude varying from 4 to 7 m. There is a slight increase in strike slip at a distance of 160 km in the middle segment of Beichuan fault (see Figure 4c). Comparing these slip patterns with the reported damage distribution lends further support to the best fitting model. The high-slip areas correlate spatially with the two devastated regions in the Longmen Shan fault zone: one is about 260 km along the Beichuan fault (to the northeast of the epicenter area), corresponding to the Wenchuan county, and the other is about 160 km along the Beichuan fault, corresponding to the Beichuan county.

[23] We compared other available coseismic slip models with our best fitting model. Our model is in general agreement with the teleseismic inversion suggesting that the earthquake involved both thrust and right-lateral strike slip [*Ji and Hayes*, 2008]. One major difference is that the teleseismic inversion did not show a significant amount of shallow (depth less than 5–8 km) slip. Teleseismic inversions have poorer depth resolution, especially within the upper crust, in contrast to the spatially dense geodetic data. Both our model and the bifault model [*Hao et al.*, 2009], which is based on ascending interferograms only, indicate large thrust at YingXiu, Houshenggou, and Bajiaomiao on

southern Beichuan fault and dominant right-lateral strike slip at Pingtong and Nanba on northern Beichuan fault (see Figure 4). In contrast, our joint inversion shows that the large-amplitude thrust near the epicentral area is shallower and the thrust component on the Pengguan fault is larger. The descending track interferograms and the GPS data resolved the ambiguity in the combined horizontal and vertical motion caused by single radar look direction.

[24] Resolving the slip partitioning between the parallel fault strands is difficult given their proximity and the fact that the interferograms are completely decorrelated in the near field, presumably due to extreme ground shaking and high strain. The estimated slip on the Pengguan fault is less robust due to the ambiguity in this slip partitioning (Figures 4a and 4b). On one hand, imposing the positivity constraint on strike-slip direction is largely redundant because the data are adequate to constrain the overall sense of motion. Relaxing the positivity constraint on strike slip results in only two small areas on the Pengguan fault and southern end of middle Beichuan fault where the slip becomes left lateral (see Figures 4a and 4c). On the other hand, such a reversal suggests that this part of the model is less well resolved. An additional complexity is the Xiaoyudong fault (a cross fault) near the epicentral region reported to have thrust slip of 1 m and left-lateral strike slip of 1 m at the surface [*Liu-Zeng et al.*, 2009]. Unfortunately, there is no available geodetic data close enough to the fault zone to resolve the motion on this cross fault. We decide not to use this cross fault after carrying out a resolution test on several different fault models (Appendix B). The deformation gradient near the surface rupture is very high as indicated by the tightly packed phase fringes close to the faults (Figures 2, 3a, and 3b). As shown in Figures 3 and 7, our best fitting model somewhat underestimates the deformation on the footwall. In Figure 3, there are positive residuals as high as 15 cm narrowly distributed along the fault. Similarly, in Figure 7, the asymmetry of the histograms reveals that there is more subsidence on the footwall than predicted. This systematic misfit might be due to a combination of complicated near-field deformation, postseismic deformation, and oversimplified fault geometry.

[25] We performed a series of checkerboard tests (Appendix B) to investigate the spatial resolution of our inversions. As anticipated, the slip distribution inferred from geodetic data has better resolution at shallow depth (Figure B1). Figure 10 shows the slip versus depth profile for each fault segment along with the aftershocks. An interesting inference is that the slip magnitude decreases rapidly with depth and is concentrated in the upper 10 km of the crust (see Table 3 and Figure 10). We tested the robustness of the model by altering top patch size (from 4 km by 8 km to 1 km by 2 km), and perturbing the smoothing and weighting parameters. The depth distribution of geodetic potency is similar to that of total slip magnitude in different fault discretization schemes. The depth-dependent slip showed stable and consistent characteristic throughout the inversions. Judging by the depths where slips drop to half of their maximums, the four fault segments behave differently. The slip is shallower in the central segment of Beichuan fault (8 km) and is deeper toward both ends (see Table 3 and Figure 10). The rupture

on Pengguan fault is extremely shallow, on average at depth of 3 to 4 km, which can be explained by the imbricate fault geometry showing that the Pengguan fault intersects and converges with Beichuan fault at depth [*Hubbard and Shaw*, 2009].

[26] Although the shallowest part of the rupture is not well constrained due to decorrelation on the hanging wall near the fault, the slip distribution shown in Figure 10 appear to be qualitatively different from the slip distribution of well-imaged magnitude ~7 strike-slip earthquakes characterized by the so-called "shallow slip deficit" [*Simons et al.*, 2002; *Fialko et al.*, 2005]. One possibility is that great earthquakes on mature faults are qualitatively different from smaller earthquakes on immature or infrequently slipping faults in that the former are able to drive slip in the shallow velocity strengthening part of the brittle layer [*Tse and Rice*, 1986; *Marone*, 1998; *Fialko*, 2004a]. The slip versus depth profile (shown in Figure 10) provides insight into the long-term strain accumulation on the Longmen Shan fault. Comparing this coseismic model with interseismic and postseismic slip models may shed light on fault behavior throughout the earthquake cycle. An alternative explanation for the prominent shallow slip in the Wenchuan earthquake is that the continental thrust events are different in rupture mode compared to the continental strike-slip events. The geodetic and seismic inversion of the Kashmir 2005 earthquake (M_w 7.6 thrusting event) showed similar kind of behavior as the Wenchuan earthquake: the slip mainly occurred in the upper 10 km of the crust [*Avouac et al.*, 2006; *Pathier et al.*, 2006].

[27] The relocated aftershocks mostly occurred at depth between 10 km and 20 km where the coseismic slip decays considerably (Figure 10). The seismicity vanishes below 25 km. As one can gather from Figure 9, the aftershocks appear to be distributed on the periphery of the area of high slip. This pattern has been observed in previous studies of significant earthquakes, such as the 2004 Bam earthquake [*Funning et al.*, 2005; *Tatar et al.*, 2005], 2007 Nias-Simeulue earthquake [*Hsu et al.*, 2006] and 2004 Parkfield earthquake [*Johanson et al.*, 2006; *Thurber et al.*, 2006; *Barbot et al.*, 2009].

5. Conclusions

[28] A coseismic slip model for the 2008 Wenchuan earthquake has been developed based on a combination of line-of-sight displacement from 41 (39 normal mode ascending and 2 ScanSAR to ScanSAR descending) ALOS interferograms, 109 GPS displacement vectors and geologic scarp height measurements. Our InSAR data provided a nearly complete coverage of the surface deformation along both ascending and descending orbits. Our best fitting model suggests the geodetic moment of 6.79×10^{20} N m to be in general agreement with the seismic moment (7.6×10^{20} N m). Fault motion was nearly equally partitioned between dip slip and right-lateral strike slip. The slip was mostly thrust in the southern segment of the Beichuan fault; then the rupture progressively changed to right-lateral strike slip as it propagated northeast. Our inversions suggest that the slip magnitude decreased with depth and concentrated in the upper 10 km of the crust. The aftershocks of the Wenchuan earthquake primarily occurred below the area of coseismic slip.

Appendix A: ScanSAR to ScanSAR Interferometry

[29] The systematic observation strategy of ALOS PALSAR provides strip-mode SAR imagery along every ascending orbital track and ScanSAR imagery along every third descending orbital track. Therefore, to obtain a second look direction of PALSAR interferometry usually requires processing ScanSAR to ScanSAR mode interferograms. Since this mode of processing is rather new for ALOS and there are few examples, we provide an overview of the method used to compute the interferogram shown in Figure A2b. The method is based on the proposal by *Bamler and Eineder* [1996] that with proper preprocessing, standard strip-mode software can be used to construct phase-preserving SAR images and ultimately interferograms. The main advantage of using the standard strip-mode approach, instead of the traditional SPECAN approach [*Sack and Cumming*, 1985], is that existing and well tested, strip-mode InSAR processing software can be used. The main disadvantage of this approach is that the zero padding between the bursts wastes considerable disk space and computer time. Nevertheless the two approaches should provide equivalent results.

[30] Our preprocessor was developed and tested using data along a descending orbital track (T538) over southern California. This track contains two permanently installed radar corner reflectors that are used by JAXA to provide radiometric and geometric calibration for ALOS for the lifetime of the mission. JAXA has collect PALSAR data over these reflectors in a variety of modes on both ascending and descending tracks. In a previous study [*Sandwell et al.*, 2008] we used the data along the ascending orbit T213 to develop a preprocessor for strip-mode interferometry including FBD to FBS interferometry. In addition we examined the noise characteristics of all combinations of FBD and FBS strip-mode interferometry and compared this noise with C band interferometry. Our main conclusion was that although the wavelength of PALSAR is 4 times longer than ERS, the RMS of the phase noise in terms of line-of-sight displacement is only 1.6 times worse (3.3 mm versus 2.1 mm). In both cases the atmospheric contribution to the phase noise dominates.

[31] Here we extend the ALOS preprocessing software to first perform ScanSAR to FBD mode interferometry and second to perform the more challenging ScanSAR to ScanSAR interferometry where a significant burst overlap is needed. Indeed, both luck and accuracy are required to achieve a full swath width ScanSAR to ScanSAR interferogram. The ScanSAR acquisition geometry and parameters for PALSAR are provided in Figure A1 and Table A1. The five subswaths cover an area ~350 km wide. Following *Bamler and Eineder* [1996], the ScanSAR data are zero-padded to construct swath type data. The original WB1 file contains the burst of all five subswaths as consecutive rows. The preprocessor separates the data into five separate files where missing lines between the bursts are filled with zeros. Zeros are also added to the end of each echo to match the length of a standard FBD data file. In addition, the first 12 lines of each burst are zero-padded because

Figure A1. Pattern of bursts for the five subswaths of PALSAR in WB1 mode. Subswath 4 corresponds to the nominal FBD and FBS strip mode imagery.

these data are incorrect (M. Shimada, personal communication, 2008). Since the subswaths are processed independently and their amplitude and interferometric phase are recombined in the latitude-longitude coordinate system, an accurate geometric model, precise orbit, and consistent set of processing parameters are required to achieve a seamless recombination. The preprocessing code is rather complex because the pulse repetition frequency (PRF) of the PALSAR echoes varies in three ways. First, as shown in Table A1, each subswath has its own PRF optimized to reduce crosstalk. Second, the PRF can change along the satellite track on any one of the subswaths. A PRF change on any subswath changes the time interval and number of zero-padded lines needed on all the other subswaths. Finally, when considering reference and repeat images for interferometry, the PRFs on a matching subswath can be different causing the burst alignment to change along the swath as we find in the example below. In addition, each subswath has its own rear range which varies along the track so rows must be shifted to align the rear range to the common prescribed value. Any small error in the preprocessing could result in a poorly focused image and/or low interferometric coherence.

[32] The first step in the software development was to focus the raw subswath data to form seamless amplitude imagery. We found that the best image quality (i.e., minimal scalloping) was achieved by setting the length of the synthetic aperture to be exactly six bursts. This corresponds to setting the time (~4.7 s) and along-track distance of synthetic aperture to be exactly the same for each subswath. We have found that by processing the SAR image to zero Doppler, the position of the radar corner reflectors in the image matches the position predicted from the orbit (zero range rate) to within 1 pixel in range and 4 pixels in azimuth. This good match provided confidence that the code is geometrically accurate.

[33] The second step in the software development was to construct ScanSAR to swath mode interferometry. This combination should always provide interference fringes because there is 100% overlap between the sparse bursts of the ScanSAR and the complete coverage of the swath [*Bertran Ortiz and Zebker*, 2007]. The ALOS track 538 over Los Angeles has two FBD acquisitions and three ScanSAR WB1 acquisitions. The swath of the FBD data (34.3° incidence angle) overlaps with subswath 4 of the WB1 data.

We experimented with three interferometric mode combinations: FBD to FBD, FBD to ScanSAR, and ScanSAR to ScanSAR. The FBD to FBD interferogram had a 10 m baseline and 46 day time span resulting in excellent overall coherence [*Zebker and Villasenor,* 1992] of 0.67. The FBD to ScanSAR interferogram had a somewhat longer baseline (121 m) and a 181 day time span resulting in a rather low average coherence of 0.24. An additional reason for the low coherence is that because of limitations in our software, we did not zero the rows in the raw FBD swath data that were aligned with the zero-padded rows in the ScanSAR data [*Bertran Ortiz and Zebker*, 2007].

[34] The third step in the software development was to construct ScanSAR to ScanSAR interferometry. The major issue here is that there is only a 20% chance of having along-track alignment of the bursts between reference and repeat orbits. There is a question of how much overlap of the bursts is needed to obtain interpretable interference fringes. We were very fortunate that two of the ScanSAR images along track 538 have significant burst overlap (up to 78%) and a moderate baseline of 450 m. An interesting aspect of this interferometric pair is that they have different PRF. This produces a gradual change in burst alignment along the track from 78% at the start of the acquisition to 0% overlap after 18 bursts. The phase and coherence of subswath 4 of this interferogram are shown in Figure A2. Phase recovery and coherence are best at the top of the swath and gradually worsen toward the bottom. A plot of row-averaged coherence versus first overlap fraction (Figure A2c) illustrates that a maximum coherence of about 0.35 occurs where the burst overlap is greater than 50%. The coherences diminish to below 0.2 at a burst overlap of 18%. The results show that

Table A1. Nominal Radar Parameters for Each Subswath

	SW1	SW2	SW3	SW4	SW5
Near range (m)	730,097	770,120	806,544	848,515	878,195
PRF (Hz)	1,692	2,370	1,715	2,160	1,916
Number of bursts[a]	247	356	274	355	327
dt (s)	0.146	0.150	0.160	0.164	0.171
Number of samples	4,976	4,720	5,376	4,432	4,688
Off nadir (deg)	20.1	26.1	30.6	34.1	36.5

[a]The number of echoes in a burst is the only fixed parameter.

(a)

(b)

(c)

T538 - subswath 1

Figure A2. ScanSAR to ScanSAR interferogram for subswath 4 of track 538 across the Los Angeles basin. The perpendicular baseline is 450 m, and the time interval is 92 days. No topographic phase has been removed. (a) Interferometric phase is high at top of swath where burst overlap is large and lower toward the bottom. (b) Coherence also decreases from top to bottom as burst overlap decreases. (c) Row-averaged coherence versus burst overlap.

good interferometric results can be achieved when the burst overlap is greater than about 50%. Assuming there is no control on the burst alignment of reference and repeat images there is a 1 in 5 chance of this occurring from any two ScanSAR images. We apply probability theory to show that five repeat SAR images will be needed to have a 90% chance of getting half burst overlap for at least one pair interferogram (Table A2). One successful alignment with

Table A2. Probability Analysis on Getting Half Burst Alignment

Number of SAR Images	Number of Interferometry Pairs	Probability of Getting at Least One Pair With Half Burst Alignment
2	1	0.2
3	3	0.488
4	6	0.7379
5	10	0.8926
6	15	0.9648
7	21	0.9908
8	28	0.9981

half burst is called an event, of which the probability is 20%. We know these events are independent but not disjoint with each other. The probability for multiple SAR images can be generalized with calculation on probability of the union.

[35] In the case of the track 124 spanning the Wenchuan earthquake there are seven ScanSAR acquisitions. We were very fortunate that there is 80% burst alignment between the reference and repeat images most closely bracketing the earthquake (Figure 2b). The time interval of this pair is 138 days and the baseline is rather long (657–844 m for perpendicular baseline) so removal of topographic phase was problematic, especially in the mountainous areas.

[36] The program used to preprocess the WB1 data into pseudostrip-mode data is available as part of an ALOS preprocessing package (available at http://www-rohan.sdsu. edu/~mellors).

Appendix B: Resolution Test

[37] We conducted a set of synthetic checkerboard tests to assess qualitatively the model resolution (Figure B1). After visually examining and comparing corresponding slip features of the checkerboard test results; we found that the slip partitioning between Beichuan and Pengguan faults is not well constrained since there are no geodetic data available to distinguish slip motion between the two parallel faults. Nevertheless, this test gives confirmation to the shallow slip in our final model. We also found that descending interferogram has great importance in resolving spatially variable slip distributions. GPS-only based inversions result in poorer resolution of the coseismic slip model than InSAR data in that the surface displacement measurements provided by GPS have wider spacing than InSAR. In the case of the final inversion, GPS data set is generally compatible with our InSAR data set.

[38] We generated the synthetic InSAR and GPS data caused by an artificial slip model, while retaining all the parameter settings as were used in making final model. Different faulting types are tested, including right-lateral strike-slip fault, thrust fault, and a combination of these two. The slip magnitude in this checkerboard test were set to be
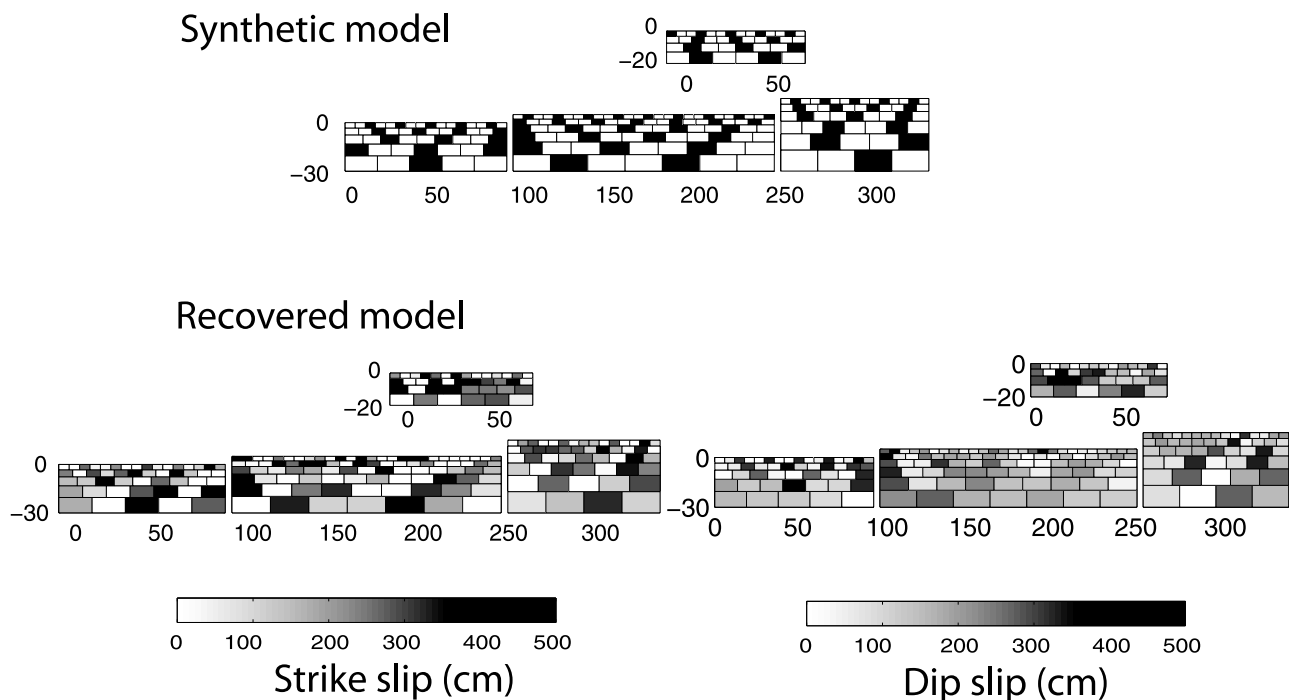
Figure B1. Checkerboard test on resolution of the inversion. The generated synthetic model has displacement of either zero or 500 cm at intervals for both the right-lateral strike-slip and dip-slip components. Then we simulated the LOS radar data, GPS data, and scarp measurement and inverted for the best fitting recovered models.

uniform (5 m), then we inverted these data to see how well the features are resolved. The smoothness was adjusted accordingly.

[39] We also tested the resolution on slip depth for three cases: 2, 9, and 20 km in width of the fault. We generated a uniform slip (5 m dextral strike slip, 5 m reverse dip slip) localized in those depth, and inverted the synthetic InSAR and GPS data to see whether this slip depth is resolved. The result shows that the resolving power with respect to slip depth is generally good. It is resolved with an error of one depth layer or less, except for the area where two parallel faults interfere with each other. This test confirms the shallow slip feature we found in our final slip model.

References

Avouac, J. P., F. Ayoub, S. Leprince, O. Konca, and D. V. Helmberger (2006), The 2005, M_w 7.6 Kashmir earthquake: Sub-pixel correlation of ASTER images and seismic waveforms analysis, *Earth Planet. Sci. Lett.*, *249*(3–4), 514–528, doi:10.1016/j.epsl.2006.06.025.

Bamler, R., and M. Eineder (1996), ScanSAR processing using standard high precision SAR algorithms, *IEEE Trans. Geosci. Remote Sens.*, *34*(1), 212–218, doi:10.1109/36.481905.

Barbot, S., Y. Fialko, and Y. Bock (2009), Postseismic deformation due to the M_w 6.0 2004 Parkfield earthquake: Stress-driven creep on a fault with spatially variable rate-and-state friction parameters, *J. Geophys. Res.*, *114*, B07405, doi:10.1029/2008JB005748.

Bertran Ortiz, A. B., and H. Zebker (2007), ScanSAR-to-Stripmap mode interferometry processing using ENVISAT/ASAR data, *IEEE Trans. Geosci. Remote Sens.*, *45*(11), 3468–3480, doi:10.1109/TGRS.2007. 895970.

Burchfiel, B. C., L. H. Royden, R. D. van der Hilst, B. H. Hager, Z. Chen, R. W. King, C. Li, J. Lu, H. Yao, and E. Kirby (2008), A geological and geophysical context for the Wenchuan earthquake of 12 May 2008, Sichuan, People's Republic of China, *GSA Today*, *18*(7), 4–11, doi:10.1130/GSATG18A.1.

Chen, Z., B. C. Burchfiel, Y. Liu, R. W. King, L. H. Royden, W. Tang, E. Wang, J. Zhao, and X. Zhang (2000), Global Positioning System measurements from eastern Tibet and their implications for India/Eurasia intercontinental deformation, *J. Geophys. Res.*, *105*(B7), 16,215–16,227, doi:10.1029/2000JB900092.

Delouis, B., D. Giardini, P. Lundgren, and J. Salichon (2002), Joint inversion of InSAR, GPS, teleseismic, and strong-motion data for the spatial and temporal distribution of earthquake slip: Application to the 1999 Izmit mainshock, *Bull. Seismol. Soc. Am.*, *92*(1), 278–299, doi:10.1785/0120000806.

Densmore, A. L., M. A. Ellis, Y. Li, R. J. Zhou, G. S. Hancock, and N. Richardson (2007), Active tectonics of the Beichuan and Pengguan faults at the eastern margin of the Tibetan Plateau, *Tectonics*, *26*, TC4005, doi:10.1029/2006TC001987.

Farr, T. G., et al. (2007), The Shuttle Radar Topography Mission, *Rev. Geophys.*, *45*, RG2004, doi:10.1029/2005RG000183.

Fialko, Y. (2004a), Probing the mechanical properties of seismically active crust with space geodesy: Study of the coseismic deformation due to the 1992 M_w 7.3 Landers (southern California) earthquake, *J. Geophys. Res.*, *109*, B03307, doi:10.1029/2003JB002756.

Fialko, Y. (2004b), Evidence of fluid-filled upper crust from observations of postseismic deformation due to the 1992 M_w 7.3 Landers earthquake, *J. Geophys. Res.*, *109*, B08401, doi:10.1029/2004JB002985.

Fialko, Y., M. Simons, and D. Agnew (2001), The complete (3-D) surface displacement field in the epicentral area of the 1999 M_w 7.1 Hector Mine earthquake, California, from space geodetic observations, *Geophys. Res. Lett.*, *28*(16), 3063–3066, doi:10.1029/2001GL013174.

Fialko, Y., D. Sandwell, M. Simons, and P. Rosen (2005), Three-dimensional deformation caused by the Bam, Iran, earthquake and the origin of shallow slip deficit, *Nature*, *435*(7040), 295–299, doi:10.1038/nature03425.

Funning, G. J., B. Parsons, T. J. Wright, J. A. Jackson, and E. J. Fielding (2005), Surface displacements and source parameters of the 2003 Bam (Iran) earthquake from Envisat advanced synthetic aperture radar imagery, *J. Geophys. Res.*, *110*, B09406, doi:10.1029/2004JB003338.

Goldstein, R. M., and C. L. Werner (1998), Radar interferogram filtering for geophysical applications, *Geophys. Res. Lett.*, *25*(21), 4035–4038, doi:10.1029/1998GL900033.

Goldstein, R. M., H. A. Zebker, and C. L. Werner (1988), Satellite radar interferometry: Two-dimensional phase unwrapping, *Radio Sci.*, *23*(4), 713–720, doi:10.1029/RS023i004p00713.

Hao, K. X., H. J. Si, H. Fujiwara, and T. Ozawa (2009), Coseismic surface-ruptures and crustal deformations of the 2008 Wenchuan earthquake M_w 7.9, China, *Geophys. Res. Lett.*, *36*, L11303, doi:10.1029/2009GL037971.

Hearn, E. H., R. Burgmann, and R. E. Reilinger (2002), Dynamics of Izmit earthquake postseismic deformation and loading of the Duzce earthquake hypocenter, *Bull. Seismol. Soc. Am.*, *92*(1), 172–193, doi:10.1785/0120000832.

Hernandez, B., F. Cotton, and M. Campillo (1999), Contribution of radar interferometry to a two-step inversion of the kinematic process of the 1992 Landers earthquake, *J. Geophys. Res.*, *104*(B6), 13,083–13,099, doi:10.1029/1999JB900078.

Hsu, Y. J., M. Simons, J. P. Avouac, J. Galetzka, K. Sieh, M. Chlieh, D. Natawidjaja, L. Prawirodirdjo, and Y. Bock (2006), Frictional afterslip following the 2005 Nias-Simeulue earthquake, Sumatra, *Science*, *312*(5782), 1921–1926, doi:10.1126/science.1126960.

Huang, Y., J. P. Wu, T. Z. Zhang, and D. N. Zhang (2008), Relocation of the *M*8.0 Wenchuan earthquake and its aftershock sequence, *Sci. China, Ser. D*, *51*(12), 1703–1711, doi:10.1007/s11430-008-0135-z.

Hubbard, J., and J. H. Shaw (2009), Uplift of the Longmen Shan and Tibetan plateau, and the 2008 Wenchuan (*M* = 7.9) earthquake, *Nature*, *458*(7235), 194–197, doi:10.1038/nature07837.

Ji, C., and G. Hayes (2008), Preliminary result of the May 12, 2008 M_w 7.9 eastern Sichuan, China earthquake, U.S. Geol. Surv., Reston, Va. (Available at http://earthquake.usgs.gov/eqcenter/eqinthenews/2008/us2008ryan/finite_fault.php)

Johanson, I. A., E. J. Fielding, F. Rolandone, and R. Burgmann (2006), Coseismic and postseismic slip of the 2004 Parkfield earthquake from space-geodetic data, *Bull. Seismol. Soc. Am.*, *96*(4b), S269–S282, doi:10.1785/0120050818.

King, G. C. P., R. S. Stein, and J. Lin (1994), Static stress changes and the triggering of earthquakes, *Bull. Seismol. Soc. Am.*, *84*(3), 935–953.

Kirby, E., K. X. Whipple, W. Q. Tang, and Z. L. Chen (2003), Distribution of active rock uplift along the eastern margin of the Tibetan Plateau: Inferences from bedrock channel longitudinal profiles, *J. Geophys. Res.*, *108*(B4), 2217, doi:10.1029/2001JB000861.

Kobayashi, T., Y. Takada, M. Furuya, and M. Murakami (2009), Locations and types of ruptures involved in the 2008 Sichuan earthquake inferred from SAR image matching, *Geophys. Res. Lett.*, *36*, L07302, doi:10.1029/2008GL036907.

Lawson, C. L., and R. J. Hanson (1974), *Solving Least Squares Problems*, Prentice Hall, Englewood Cliffs, N. J.

Liu-Zeng, J., et al. (2009), Co-seismic ruptures of the 12 May 2008, M_s 8.0 Wenchuan earthquake, Sichuan: East-west crustal shortening on oblique, parallel thrusts along the eastern edge of Tibet, *Earth Planet. Sci. Lett.*, *286*(3–4), 355–370, doi:10.1016/j.epsl.2009.07.017.

Marone, C. (1998), Laboratory-derived friction laws and their application to seismic faulting, *Annu. Rev. Earth Planet. Sci.*, *26*, 643–696, doi:10.1146/annurev.earth.26.1.643.

Massonnet, D., and K. L. Feigl (1998), Radar interferometry and its application to changes in the Earth's surface, *Rev. Geophys.*, *36*(4), 441–500, doi:10.1029/97RG03139.

Meyer, F., R. Bamler, N. Jakowski, and T. Fritz (2006), The potential of low-frequency SAR systems for mapping ionospheric TEC distributions, *IEEE Geosci. Remote Sens. Lett.*, *3*(4), 560–564, doi:10.1109/LGRS.2006.882148.

Okada, Y. (1985), Surface deformation due to shear and tensile faults in a half-space, *Bull. Seismol. Soc. Am.*, *75*(4), 1135–1154.

Parker, R. L. (1994), *Geophysical Inverse Theory*, Princeton Univ. Press, Princeton, N. J.

Pathier, E., E. J. Fielding, T. J. Wright, R. Walker, B. E. Parsons, and S. Hensley (2006), Displacement field and slip distribution of the 2005 Kashmir earthquake from SAR imagery, *Geophys. Res. Lett.*, *33*, L20310, doi:10.1029/2006GL027193.

Perfettini, H., and J. P. Avouac (2007), Modeling afterslip and aftershocks following the 1992 Landers earthquake, *J. Geophys. Res.*, *112*, B07409, doi:10.1029/2006JB004399.

Pollitz, F. F., G. Peltzer, and R. Burgmann (2000), Mobility of continental mantle: Evidence from postseismic geodetic observations following the 1992 Landers earthquake, *J. Geophys. Res.*, *105*(B4), 8035–8054, doi:10.1029/1999JB900380.

Price, E. J., and D. T. Sandwell (1998), Small-scale deformations associated with the 1992 Landers, California, earthquake mapped by synthetic aperture radar interferometry phase gradients, *J. Geophys. Res.*, *103*(B11), 27,001–27,016, doi:10.1029/98JB01821.

Rosenqvist, A., M. Shimada, N. Ito, and M. Watanabe (2007), ALOS PAL-SAR: A Pathfinder mission for global-scale monitoring of the environment, *IEEE Trans. Geosci. Remote Sens.*, *45*(11), 3307–3316, doi:10.1109/TGRS.2007.901027.

Sack, M., and I. G. Cumming (1985), Application of efficient linear fm matched filtering algorithms to synthetic aperture radar processing, *IEE Proc. Part F Radar Signal Processing*, *132*(1), 45–57.

Saito, A., M. Nishimura, M. Yamamoto, S. Fukao, T. Tsugawa, Y. Otsuka, S. Miyazaki, and M. C. Kelley (2002), Observations of traveling ionospheric disturbances and 3-m scale irregularities in the nighttime *F* region ionosphere with the MU radar and a GPS network, *Earth Planets Space*, *54*, 31–44.

Sandwell, D. T., L. Sichoix, and B. Smith (2002), The 1999 Hector Mine earthquake, southern California: Vector near-field displacements from ERS InSAR, *Bull. Seismol. Soc. Am.*, *92*(4), 1341–1354, doi:10.1785/0120000901.

Sandwell, D. T., D. Myer, R. Mellors, M. Shimada, B. Brooks, and J. Foster (2008), Accuracy and resolution of ALOS interferometry: Vector deformation maps of the Father's Day intrusion at Kilauea, *IEEE Trans. Geosci. Remote Sens.*, *46*(11), 3524–3534, doi:10.1109/TGRS.2008.2000634.

Simons, M., Y. Fialko, and L. Rivera (2002), Coseismic deformation from the 1999 M_w 7.1 Hector Mine, California, earthquake as inferred from InSAR and GPS observations, *Bull. Seismol. Soc. Am.*, *92*(4), 1390–1402, doi:10.1785/0120000933.

Tatar, M., D. Hatzfeld, A. S. Moradi, and A. Paul (2005), The 2003 December 26 Bam earthquake (Iran), M_w 6.6, aftershock sequence, *Geophys. J. Int.*, *163*(1), 90–105, doi:10.1111/j.1365-246X.2005.02639.x.

Thurber, C., H. J. Zhang, F. Waldhauser, J. Hardebeck, A. Michael, and D. Eberhart-Phillips (2006), Three-dimensional compressional wave-speed model, earthquake relocations, and focal mechanisms for the Park-field, California, region, *Bull. Seismol. Soc. Am.*, *96*(4b), S38–S49, doi:10.1785/0120050825.

Tong, X., D. T. Sandwell, Y. Fialko, and R. J. Mellors (2008), Coseismic displacement of *M*8.0 Sichuan earthquake derived by ALOS radar interferometry, *Eos Trans. AGU*, *89*(53), Fall Meet Suppl., Abstract G33C-0715.

Tse, S. T., and J. R. Rice (1986), Crustal earthquake instability in relation to the depth variation of frictional slip properties, *J. Geophys. Res.*, *91*(B9), 9452–9472, doi:10.1029/JB091iB09p09452.

Wessel, P., and W. H. F. Smith (1998), New, improved version of the Generic Mapping Tools Released, *Eos Trans. AGU*, *79*, 579, doi:10.1029/98EO00426.

Working Group of the Crustal Motion Observation Network of China Project (2008), The coseismic displacement of 2008 Wenchuan M_s8.0 earthquake measured by GPS (in Chinese), *Sci. China, Ser. D*, *38*(10), 1195–1206.

Zebker, H. A., and J. Villasenor (1992), Decorrelation in interferometric radar echoes, *IEEE Trans. Geosci. Remote Sens.*, *30*(5), 950–959, doi:10.1109/36.175330.

Zebker, H. A., P. A. Rosen, R. M. Goldstein, A. Gabriel, and C. L. Werner (1994), On the derivation of coseismic displacement fields using differential radar interferometry: The Landers earthquake, *J. Geophys. Res.*, *99*(B10), 19,617–19,634, doi:10.1029/94JB01179.

Y. Fialko, D. T. Sandwell, and X. Tong, Institute of Geophysics and Planetary Physics, Scripps Institution of Oceanography, 9500 Gilman Dr., La Jolla, CA 92037, USA.